Selective chemical vapor deposition approach for Sb_2Te_3 thin film micro-thermoelectric generators

*Daniel W. Newbrook[a], Stephen P. Richards[b], Victoria K. Greenacre[b], Andrew L. Hector[b], William Levason[b], Gillian Reid[b], C. H. (Kees) de Groot[a] and Ruomeng Huang[a]**

[a]School of Electronics and Computer Science, University of Southampton, Southampton, SO17 1BJ, United Kingdom

[b]School of Chemistry, University of Southampton, Southampton, SO17 1BJ, United Kingdom

KEYWORDS micro-thermoelectric generator, thin film, selective chemical vapor deposition, Sb_2Te_3, single source precursor

ABSTRACT Micro-thermoelectric generators are attractive for autonomous sensor systems. This work reports an approach for fabricating thin film micro-thermoelectric generators via selective chemical vapor deposition. The approach utilizes our single source precursors which enable the production of high-quality thermoelectric materials, as exemplified by Sb_2Te_3 in this work. It also allows great control over the thermoelectric properties of the as-deposited Sb_2Te_3 by simply varying the deposition temperature. A competitive power factor of 16.5 $\mu W/cm \cdot K^2$ can be obtained for a Sb_2Te_3 films deposited at 364ºC, with the highest estimated ZT value of 0.65. The selective deposition over the conductive TiN surface enables the fabrication of a prototype single-leg

thermoelectric generator, which produces a maximum power of 0.27 nW with a temperature gradient of only 0.11K while reducing 87% of tellurium consumption.

1. Introduction

The thriving Internet of Things (IoT) and Wireless Sensor Networks (WSN) presents a new demand for sustainable power supplies to the sensor nodes and IoT embedded systems [1,2]. Development of micro-scale energy harvesting technologies is key to replace wires and batteries and realize a truly energy autonomous system. Micro-thermoelectric generators (micro-TEGs), which transforms waste heat produced daily in our society into electricity, while offering high reliability, long lifetimes, no maintenance and solid-state operation, are a promising option to produce a sustainable power supply for those devices [3,4].

Thermoelectric materials have attracted tremendous attention from many researchers in recent decades [5]. The conversion efficiency of a TE material is often evaluated by a dimensionless figure-of-merit ($ZT = S^2\sigma T/k$), where S, σ, T and k denote the Seebeck coefficient, electrical conductivity, operating temperature in Kelvin, and total thermal conductivity (containing the electrical contribution $k_{el}$and lattice contribution k_l), respectively. A large ZT value will normally mean an effective enhancement of the power factor ($PF = S^2\sigma$) and simultaneous reduction of thermal conductivity [6]. A wide range of materials have been investigated to show high *ZT* values at different temperatures. Notable examples include SiGe alloys and Half-Heusler compounds working at high temperature ranges, and PbTe-based alloys and SnSe compounds working at mid-temperature ranges [7,8]. For the application in micro-scale energy harvesting, thin film TE materials with maximum *ZT* values at room temperature are preferred. Tellurium based chalcogenides (e.g.

Bi_2Te_3, Sb_2Te_3) have been identified as the best TE materials for near room temperature applications [9]. Several deposition technologies have been used in depositing thin film TE materials, including sputtering [10], pulsed laser deposition [11], electrodeposition [12], thermal evaporation [13,14], and molecular beam epitaxy [15].

Research on micro/nano-TEGs for small scale energy harvesting has developed rapidly within recent years [16,17]. Tainoff *et al.* reported a mechanically suspended BiTeSe/BiSbTe based nanogenerator fabricated by sputtering, demonstrating a power of 0.26 nW for a single nanoTEG cell at a temperature difference of 8 K [18]. Yuan *et al.* also presented a BiTeSe/BiSbTe based radial structure micro-TEG through screen-printing, producing an output power of 5.81 μW at a temperature difference of 48.3 K [19]. Other deposition techniques, such as thermal evaporation [20], electrodeposition [21,22], zone-melting [23] and pulsed laser deposition [24] were also reported to fabricated tellurium-based micro-TEGs. However, the scarcity (low natural abundance) of tellurium is a serious concern for the mass-production of Bi_2Te_3 and Sb_2Te_3 based thermoelectric generators [25]. In light of this, several tellurium-free micro/nano-TEG have been proposed. Notable examples include recent works published on silicon integrated circuit thermoelectric generators [26], and silicon and SiGe nanowires based micro-TEGs [27–29].

Chemical vapor deposition (CVD) enables the production of thin films with superior quality compared to those obtained by sputtering in terms of conformity, coverage and stoichiometry control. Conventionally in CVD, deposition of binary or ternary compounds require multiple precursor source systems [30]. Single source precursors (SSPs) are a promising alternative for these systems, as they improve ease of handling and atom efficiency while allowing properties such as stoichiometry and morphology to be directed by precursor design. We have previously demonstrated the viabilities of using SSPs to deposit high quality binary (e.g. $SnSe_2$, $TiSe_2$, Bi_2Te_3

and Sb_2Te_3) and their compatibility to produce ternary ($Bi_2(Se_{1-x}Te_x)_3$ and $(Bi_{1-y}Sb_y)_2Te_3$) chalcogenides [31–35]. The possibility of selective deposition of oriented films onto defined regions of lithographically patterned substrates has been realised using these types of precursors for a variety of metal chalcogenide materials [36], paving the way for their application in thermoelectric energy harvesting. By eliminating the need to etch away large amounts of the films to create the array of TE elements, this robust selective deposition process could avoid the damage to materials and has the potential to significantly reduce the consumption of tellurium.

In the present study, we report the TE properties p-type Sb_2Te_3 thin films using SSP based CVD. The resultant films demonstrate high purity with thermoelectric properties comparable to the state-of-art values. An effective strategy for improving power factor to achieve high *ZT* values is by tuning the carrier concentration as it has a large influence on S, σ and k_{el} [9,37]. Here we demonstrate the potential of optimising the TE properties based on this CVD approach through tuning the deposition temperature as an effective way to optimise the carrier concentration and mobility of Sb_2Te_3 thin films, leading to an average power factor over 15 $\mu W/cm \cdot K^2$ in the temperature range from 200K to 400K. For the first time, we demonstrate that the selective deposition behaviour from our single SSP based CVD can be used to fabricate micro-TEGs.

2. Materials and methods

2.1. Single source precursor synthesis

The single source precursor $MeSb(Te^nBu)_2$ (Me = CH_3, ^nBu = n-C_4H_9) was synthesized for the deposition of Sb_2Te_3 thin films. More information about the precursor synthesis can be found in our previous work [34].

2.2. LPCVD of Sb_2Te_3

For a typical deposition, both precursor and substrates were loaded into a closed-end quartz tube in a glove-box. The precursor, normally *ca.* 70 mg, was placed at the closed end and several SiO_2-coated silicon substrates were positioned end-to-end near the precursor. After loading the substrates, the tube was set to the target deposition temperature in a furnace such that the precursor was outside the heated zone; the tube was evacuated, heated to the set temperature under 0.05 mmHg and the furnace was allowed to stabilise. The tube position was subsequently adjusted so that the precursor was moved gradually towards the hot zone until evaporation was observed. Temperature profiling along the tube was conducted for each deposition to identify the actual temperature on each substrate. The tube remained unmoved until the precursor had completely evaporated (no residue remained), i.e. *ca.* 1–3 h. After this, the tube was cooled to room temperature and transferred to the glove box where the tiles were removed and stored under an N_2 atmosphere prior to analysis.

2.3. Thin film characterisation

Scanning electron microscopy (SEM) was performed using a Zeiss EVO LS 25 with an accelerating voltage of 10 kV, and energy-dispersive X-ray (EDX) data were obtained with an Oxford INCAx-act X-ray detector. High resolution SEM measurements were carried out with a field emission SEM (Jeol JSM 7500F) at an accelerating voltage of 2 kV. X-Ray diffraction (XRD) measurements were carried out using a Rigaku Smartlab diffractometer with a 9 kW Cu-Ka source, parallel line focus incident beam and a Hypix detector. X-ray photoelectron spectroscopy (XPS) data were obtained using a ThermoScientific Theta Probe system with Al–Kα radiation (photon energy= 1486.6 eV). XPS depth profile was performed by using an Ar ion gun at a beam voltage

of 3 kV on a 2 × 2 mm raster area. Raman scattering spectra of the deposited films were measured at room temperature on a Renishaw InVia micro Raman spectrometer using a helium–neon laser with a wavelength of 633 nm. The incident laser power was adjusted to be *ca.*1 mW for all samples.

The in-plane electrical conductivity (σ) and Seebeck coefficient (S) were simultaneously measured on a commercial JouleYacht thin-film thermoelectric parameter test system (MRS-3L). The system was calibrated using a nickel foil reference standard and the measurement accuracy was found to be within 5%. The Hall coefficient (R_H) was determined at 300 K on a Nanometrics HL5500PC instrument using a van de Pauw configuration. The carrier concentration (n_H) and in-plane mobility (μ_H) were computed according to $n_H = 1/eR_H$ and $\mu_H = \sigma R_H$, respectively.

2.4. Prototype thermoelectric generator fabrication and characterisation

Patterned substrates were prepared for the fabrication of the thermoelectric generator. A 200 nm TiN bottom electrode layer was firstly patterned on a SiO_2/Si substrate by photolithography using magnetron sputtering (Leybold Optics HELIOS Pro XL). An insulating SiO_2 layer with a thickness of 500 nm was subsequently sputtered to cover the entire substrate. This was followed by a second photolithography and reactive ion etching (RIE) process to reveal the p-type leg area on the bottom electrode. These substrates were then subject to selective CVD using the single source precursor as discussed above. A similar CVD process was adopted although a much smaller precursor quantity (*ca.* 5-10 mg) was used. After the Sb_2Te_3 layer was selectively deposited in the p-type leg area, further lithography and RIE process was performed to reveal the n-type leg area. At this stage, n-type TE materials such as Bi_2Te_3 can be selectively deposited into the n-type leg area to make a full device. However, for the purpose of demonstrating the feasibility of this process, single (p) leg TEGs were fabricated. This was done by photolithographically patterning the top TiN electrode

layer with a thickness of 1000 nm connecting the empty n-type leg area and the Sb_2Te_3 filled p-type leg area. A detailed fabrication process is shown in Figure S1.

The power generation performance of the device was characterised by electrically connecting the pads of the devices to a PCB by soldering. Silver paste was used to improve the electrical contacts. Once contacted, a temperature difference was established by clamping the device between two direct-to-air Peltier devices (DT-AR-014-12), where one was used as a cooler and the other as a heater. The Peltier devices were controlled via two PID controllers, keeping the cool side constant at 20ºC and varying the hot side temperature. Once at thermal equilibrium, a potentiometer was used to vary the load resistance. Both the current and voltage were measured using a Fluke 8808A multimeter. The system was left to stabilise between each power measurement.

Device simulations were computed using COMSOL Multiphysics® using the same dimensions as in the fabricated device and thermoelectric properties from experimental results. The measurement of the temperature gradient at equilibrium is extremely challenging. In this work, the temperature gradient was calculated by the open circuit voltages and the Seebeck coefficient of Sb_2Te_3 films at corresponding temperature. The calculated temperature gradients were subsequently used in the simulations to evaluate the device performance.

3. Results and discussion

3.1. Sb_2Te_3 thin film

Figure 1a-1e present the top-view SEM images of the Sb_2Te_3 films as-deposited at different temperatures. All films appear to be polycrystalline, characterised by hexagonal crystals randomly grown on the substrate. Cross-section SEM images (Figure S2) reveal that all films are continuous

with thicknesses in the range of 1 to 3 µm. The film compositions are investigated by EDX (Figure 1f). All films are subjected to multiple EDX measurements across the entire deposition area to confirm the uniformity in composition. Spectra of all five films appear to be similar with no impurities and the Sb to Te ratios are found to be 40(2) to 60(2) in all cases. This is further confirmed by XPS measurements (Figure S3).

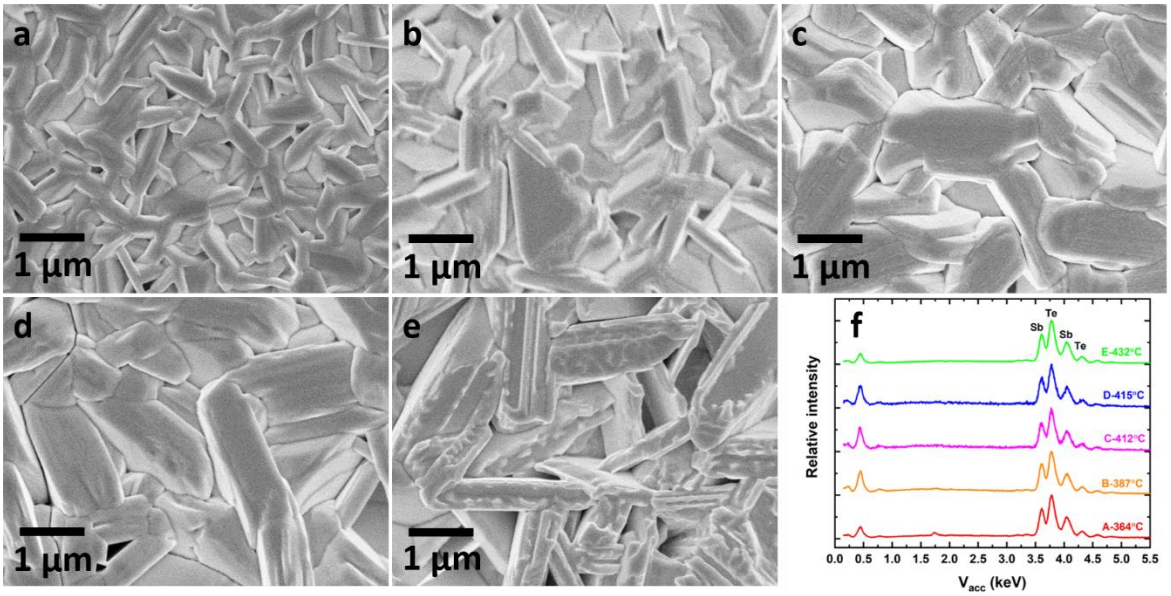

Figure 1 SEM images showing the morphologies of the Sb_2Te_3 deposited by LPCVD onto SiO_2-coated silicon substrates at temperatures of (a) 364ºC, (b) 387ºC, (c) 412ºC, (d) 415ºC, (e) 432ºC and their respective EDX spectra (f).

The structural properties were investigated by grazing incidence XRD (Figure 2). All patterns of the films show the same single phases of Sb_2Te_3 ($R\bar{3}mh$), with peak positions that correspond well with literature values [38]. Similar peak intensity ratio with no preferred orientation is observed for each film according to the XRD patterns (Figure 2a), implying the growth orientation is insensitive within the deposition temperature range The crystallite size of each film can be calculated from Scherrer's equation and is presented in Figure S4, showing no relation to the deposition temperature. The lattice parameters (a, c) of all five films are refined against the Sb_2Te_3

phases from ICSD [39], showing similar values (Figure 2b). The vibrational properties of the as-deposited Sb_2Te_3 thin films were investigated by Raman spectroscopy with spectra shown in Figure S5. Two characteristic vibrations modes E_g^2 (in-plane) and A_{1g}^2 (out-of-plane) modes are present in the five films with no obvious shift.

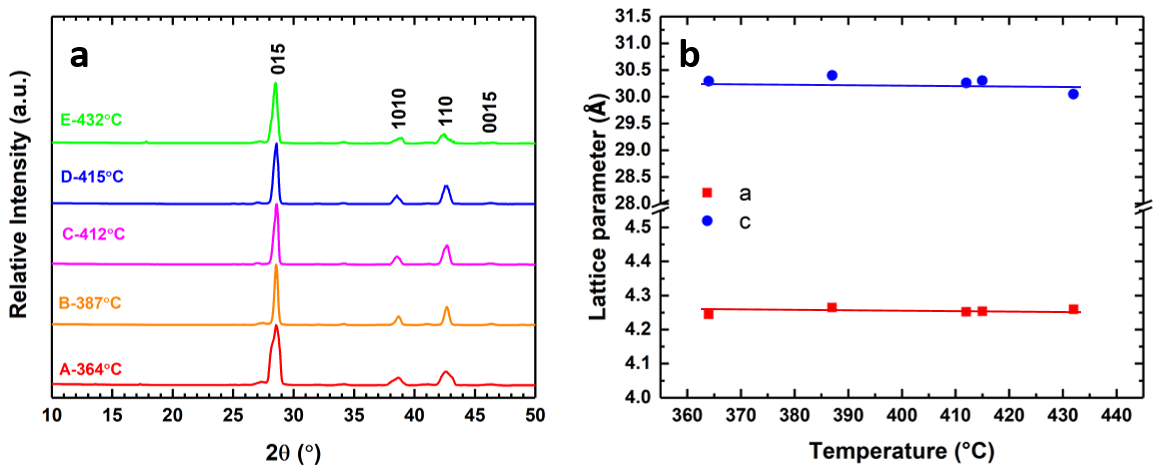

Figure 2 (a) XRD patterns of as-deposited Sb_2Te_3 deposited by LPCVD at different temperatures; (b) refined lattice parameters as a function of deposition temperature for the as-deposited Sb_2Te_3 films. The lines are guides to the eyes.

Room temperature Hall measurements (Figure 3) on these structurally identical Sb_2Te_3 films reveal significantly different electrical properties. Although all films demonstrate p-type semiconducting behaviour, the carrier concentration increases with increasing deposition temperature. The strong p-type conductivity in Sb_2Te_3 results from the dominant intrinsic point defect of Sb antisites (Sb'_{Te}) [40]. An increase of the deposition temperature further facilitates the formation of such antisites as Te is more prone to be volatile at elevated temperatures, leading to a Te-deficient condition. The formation energy of Sb antisites is considerably lower than that of Te vacancies (V''_{Te}) and is more likely to form under such conditions. It is worth pointing out that in theory, Sb'_{Te} antisite defect will increase the lattice constant on the c-axis due to the larger Sb

atom radius. However, this change is too small to be observed by both EDX and XRD. Relatively high carrier mobilities were observed for all Sb_2Te_3 films, which could largely be attributed to the relatively low carrier concentrations causing reduced ionized impurity scattering. Nevertheless, the ionized impurities still play an important role in carrier mobility as it concurrently reduces with increasing carrier concentration. Similar behaviour was also reported in other works [41,42].

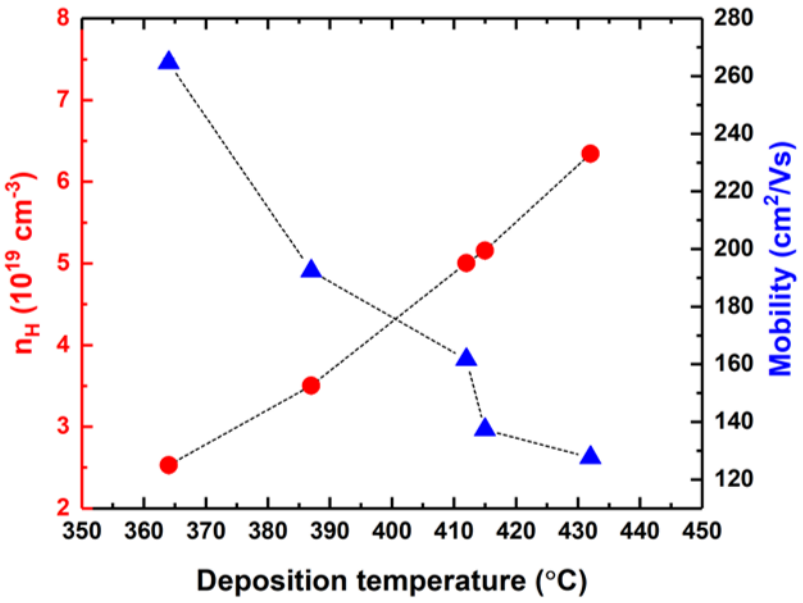

Figure 3 Room temperature carrier concentration (red circle) and mobility (blue triangle) of the as-deposited Sb_2Te_3 LPCVD films as a function of deposition temperature. The dotted lines are guides to the eyes.

The temperature dependent electrical conductivity of the five Sb_2Te_3 films are presented in Figure 4a. All films demonstrate semi-metallic conducting behaviour as the conductivity reduces with increasing temperature. A slight increase of σ is observed with increasing deposition temperature due to the dominance of the increasing carrier concentration (Figure 4b), but it is nearly compensated by the simultaneous decrease of carrier mobility. Seebeck coefficients of the as-deposited Sb_2Te_3 films are shown in Figure 4c. The positive values confirm the p-type conductivity

of those films. The Seebeck coefficient is found to be increasing with decreasing deposition temperature and carrier concertation (Figure 4d).

To further shed light on the electrical transport mechanism, the Seebeck coefficient versus carrier concentration (Pisarenko plot) at 300K is plotted in Figure 4e. A simple electron transport model is used to calculate the dotted lines, which serve as guidelines. The model can be written as:

$$S = \frac{8\pi^2 k_B^2}{3eh^2}\left(\frac{\pi}{3n}\right)^{2/3} m^* T$$

where k_B is the Boltzmann constant, h the Planck constant, and m^* the effective mass [43]. It assumes a single parabolic band and approximates energy-independent carrier scattering in degenerate semiconductors [44]. It further reveals that lower carrier concentration obtained from lower deposition temperature could reduce the density-of-state effective mass of the Sb_2Te_3 from 0.75 m_0 to 0.5 m_0 (Figure 4e-inset). In general, lower effective mass leads to lower Seebeck coefficient at the same carrier concentration level. However, it also improves the electrical conductivity through higher mobility, leading to high ZT values [45]. The power factors are shown in Figure 4f. Sb_2Te_3 films deposited at 364 ºC demonstrates the highest power factor due to high Seebeck coefficient and moderate electrical conductivity. An average power factor over 15 $\mu W/cm \cdot K^2$ in the temperature range from 200 K to 400 K is obtained which is competitive among some of the recent thin film works [46–49]. This demonstrates the capability of our SSP-based CVD in controlling and optimizing the thermoelectric properties.

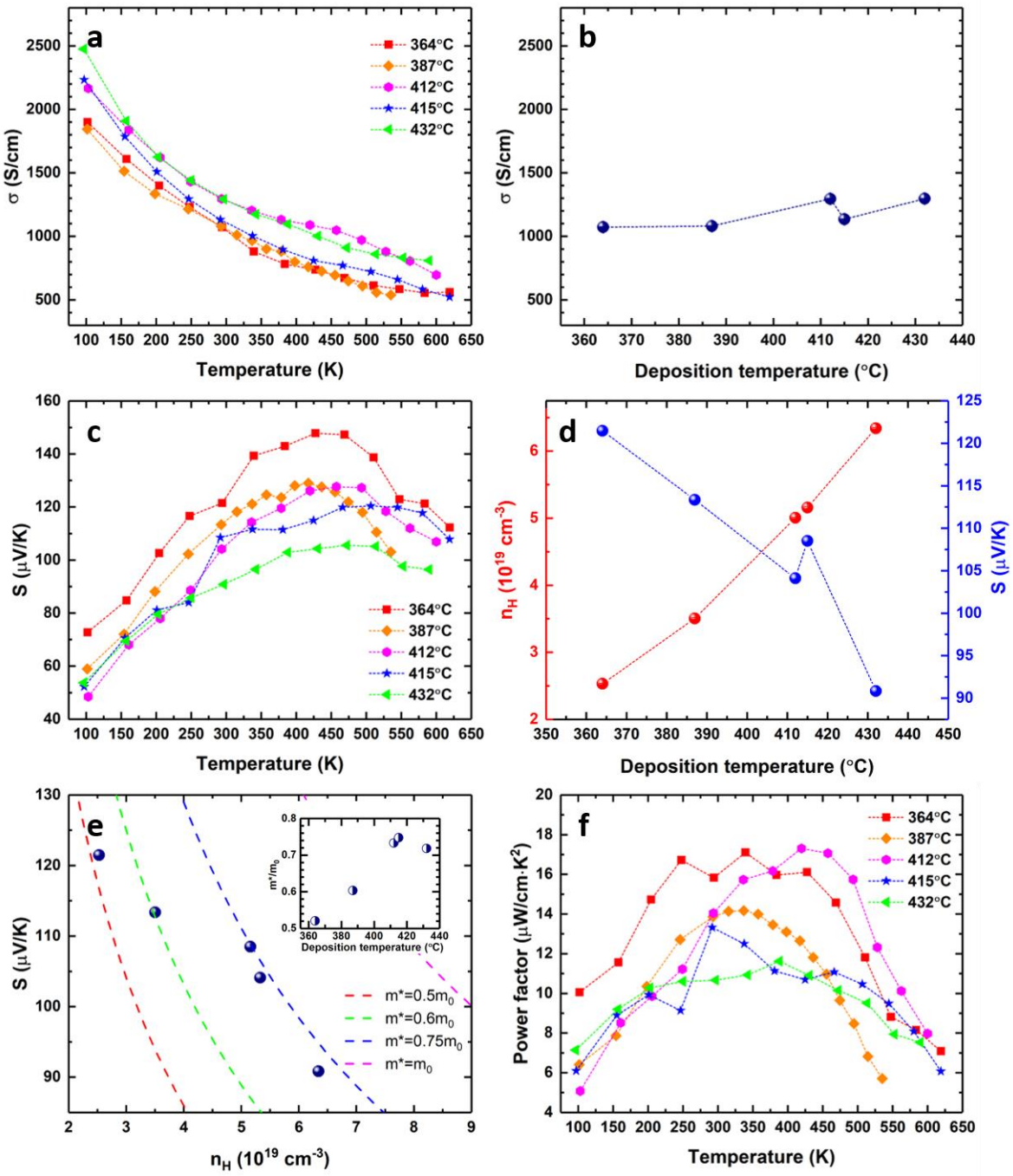

Figure 4 (a) Temperature dependent in-plane electrical conductivity of the as-deposited Sb_2Te_3 films deposited at different temperatures. (b) Room temperature electrical conductivity as a function of deposition temperature. (c) Temperature dependent in-plane Seebeck coefficient of the as-deposited Sb_2Te_3 films deposited from different temperatures. (d) Room temperature Seebeck coefficient and carrier concentration as a function of deposition temperature. (e) Room temperature Seebeck coefficient as-deposited Sb_2Te_3 films as a function of the carrier concentration (Pisarenko plot), the dotted lines represent the values calculated for $m^* = 0.5, 0.6, 0.75\ and\ 1.0\ m_e$; inset: density-of-state effective mass as a function of deposition temperature. (f) Temperature dependent in-plane power factor of the as-deposited Sb_2Te_3 films deposited at different temperatures.

Measurement of thermal conducting properties of thin films is extremely challenging and often prone to error. Here we estimate the total thermal conductivity by assuming a constant lattice contribution of 0.5 W/mK. We believe this is a relatively conservative estimation giving the small size of our crystals which help to reduce the lattice thermal conductivity by enhancing phonon-scattering [6,37,50]. The electrical contribution of the thermal conductivity (k_{el}) is calculated (Figure S6) using the Wiedemann-Franz law ($k_{el} = L\sigma T$), where is the Lorenz number and was calculated by adopting an empirical equation proposed by Snyder *et al.* [51]. The estimated figure-of-merit are presented in Figure 5 in which Sb_2Te_3 films deposited at 364ºC demonstrates the highest ZT values of 0.65 at 450K.

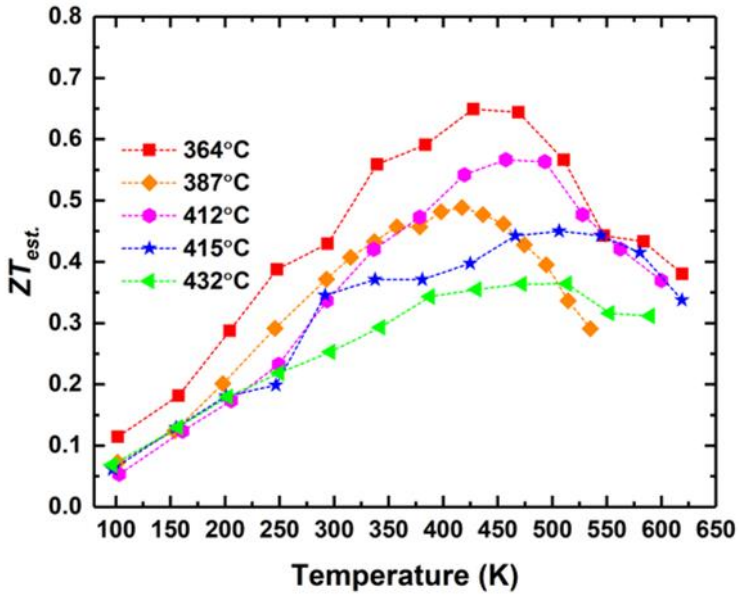

Figure 5 Estimated temperature dependent ZT of the as-deposited Sb_2Te_3 films deposited from different temperatures.

3.2. Prototype micro-TEG from selective CVD

Figure 6a presents the optical microscope image and the schematic of the prototype single-leg micro-TEG fabricated from our selective CVD process. The micro-TEG contains 72 pairs of p-n

TE legs with leg width of 200 μm. Sb_2Te_3 can be observed only inside the p-leg area due to the selective deposition behaviour, while the n-leg is filled with TiN. Adjustable temperature differences are imposed by sandwiching the micro-TEG between two commercial TE heater/cooler units. Figure 6b shows the output power of the micro-TEG at different ΔT (solid symbols). Direct measurement of ΔT is very difficult considering the dimension of the device. Here the different ΔT values were characterized by the open circuit-voltage of the generator. A higher ΔT leads to a higher power output. The maximum output power is 0.27 nW at a ΔT of 0.11K. These results are well matched to the COMSOL simulation results under the same condition (open symbols). Compared with conventional non-selective deposition technique where legs are patterned by etching Tellurium-containing thermoelectric thin films, our process could significantly reduce the amount of tellurium needed. In the device presented in this work, the consumption of tellurium is reduced to just 13% by using our selective deposition technique which is significant considering the scarcity of tellurium.

It is worth mentioning that the micro-TEG demonstrated in this work is a proof-of-concept prototype and has great potential for improvements. We have demonstrated previously that this approach has excellent scalability and the selectivity can be achieved at nanometer scale [36]. Simulations were carried out to project the power generation performance of our micro-TEG with reduced pitch. As shown in Figure 6c, over 3-order of magnitude increase of maximum power were predicted when the device pitch is decreased from 200 μm to 10 μm, reaching 500 nW, with other conditions remaining the same. This significant increase can be largely ascribed to the increase of TE pair numbers while the increase of resistance is less significant as most of the resistance arise from the interconnects. Figure 6c also presents the projected specific power generation capacity Γ_P ($P_{max}/A(\Delta T)^2$) of our micro-TEG based on simulation. A maximum Γ_P of

230 μW cm^{-2} K^{-2} was achieved which is competitive with the state-of-art TEG. Apart from pitch scaling, the power generation can be further improved by integrating a full micro-TEG with both n-type and p-type legs by this selective deposition process. The temperature gradient over the legs can also be further increased by producing longer legs which are only 500 nm in the prototype.

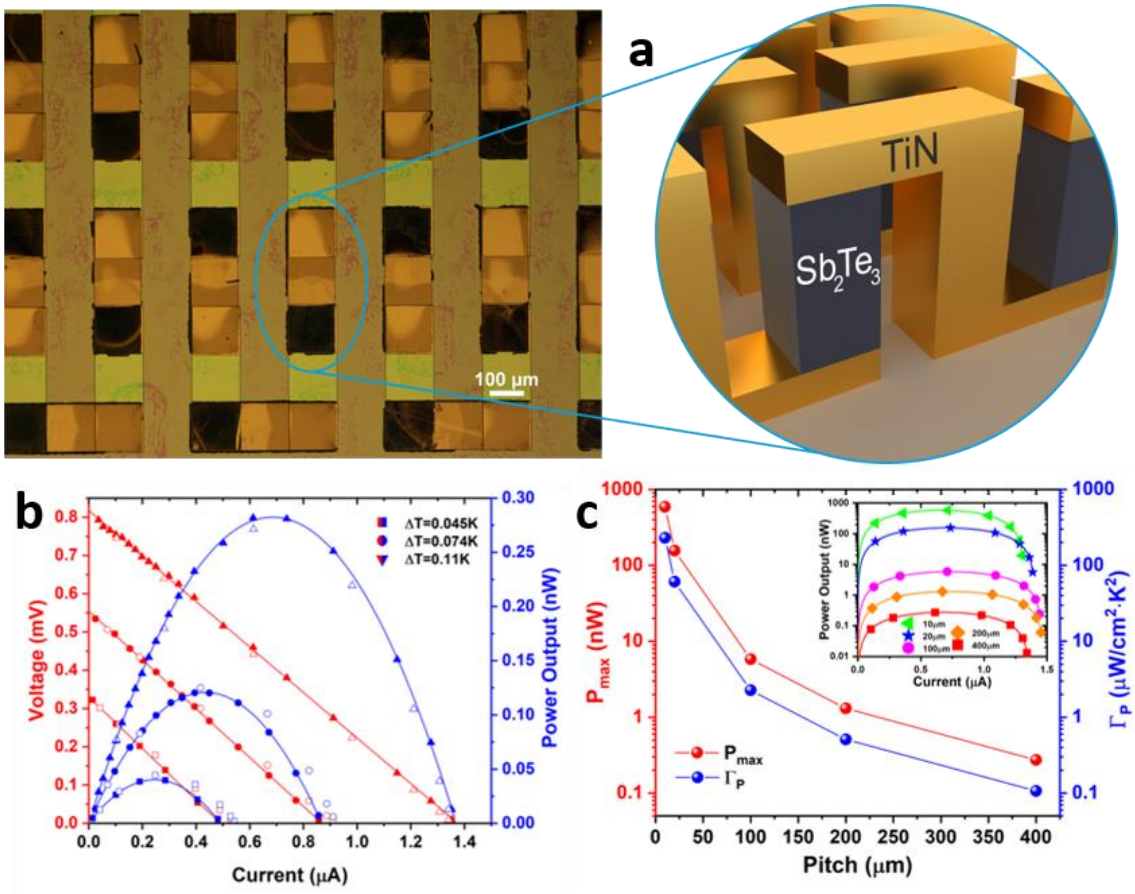

Figure 6 (a) Optical microscope image (left) and schematic (right) of the single-leg micro-TEG fabricated from selective CVD process; (b) experimental (solid symbols) and simulation (open symbol) results of output voltage (red) and power outputs (blue) produced from the single-leg micro-TEG at different temperature gradients as a function of the load current; (c) projected maximum power generation (red) and specific power generation capacity (blue) as a function of pitch. Inset: projected power outputs produced from the single-leg micro-TEG at different pitches as a function of the load current.

4. Conclusions

We have demonstrated the deposition of p-type Sb_2Te_3 thermoelectric thin films by SSP-based CVD approach. The thermoelectric properties of the as-deposited Sb_2Te_3 were tunable in this process by simply varying the deposition temperature. Lower deposition temperature supresses the formation of Sb antisite, leading to a low carrier concentration and high mobility and Seebeck coefficient. A competitive power factor of 16.5 μW/cm·K^2 has been demonstrated for a Sb_2Te_3 film deposited at 364ºC with the highest estimated ZT value of 0.65.

The unique selective deposition behaviour of this deposition approach has also been successfully used to fabricate micro-TEGs for the first time. A maximum power of 0.27 nW was achieved on a single-leg device with a temperature gradient of only 0.11K. A projected specific power generation capacity Γ_P of 230 μW cm^{-2} K^{-2} can be achieved when reducing the generator pitch from 200 μm to 10 μm. The successful demonstration of this prototype device offers exciting prospects for further developing this technique in thermoelectric applications.

ASSOCIATED CONTENT

Supporting Information.

The following files are available free of charge.

Experimental section, SEM images, XPS spectra, Raman spectra and the electrical thermal conductivity results (PDF)

AUTHOR INFORMATION

Corresponding Author

*Email: r.huang@soton.ac.uk; Tel.: +44 023 8059 9305

University Road, University of Southampton, Southampton, SO17 1BJ, United Kingdom

Funding Sources

Science and Technology Facilities Council (STFC), UK

Engineering and Physical Sciences Research Council (EPSRC), UK

Notes

The authors declare no competing financial interest.

ACKNOWLEDGMENT

We thank the STFC for funding (ST/L003376/1 and ST/P00007X/1). We also gratefully acknowledge funding for thin film diffraction and NMR instrumentation from the EPSRC through EP/K00509X, EP/K009877/1 and EP/K039466/1. DWN would like to thank both BAE and EPSRC for funding the iCASE studentship. All data supporting this study are openly available from the University of Southampton repository at DOI: https://doi.org/10.5258/SOTON/D1365.

REFERENCES

(1) Haras, M.; Skotnicki, T. Thermoelectricity for IoT – A Review. *Nano Energy* **2018**, *54*, 461–476.

(2) Raj, A.; Steingart, D. Review—Power Sources for the Internet of Things. *J. Electrochem. Soc.* **2018**, *165*, B3130–B3136.

(3) Petsagkourakis, I.; Tybrandt, K.; Crispin, X.; Ohkubo, I.; Satoh, N.; Mori, T. Thermoelectric Materials and Applications for Energy Harvesting Power Generation. *Sci. Technol. Adv. Mater.* **2018**, *19*, 836–862.

(4) Narducci, D. Thermoelectric Harvesters and the Internet of Things: Technological and Economic Drivers. *J. Phys. Energy* **2019**, *1*, 024001.

(5) Snyder, G. J.; Toberer, E. S. Complex Thermoelectric Materials. *Nat. Mater.* **2008**, *7*, 105–114.

(6) Zhou, X.; Yan, Y.; Lu, X.; Zhu, H.; Han, X.; Chen, G.; Ren, Z. Routes for High-Performance Thermoelectric Materials. *Mater. Today* **2018**, *21*, 974–988.

(7) He, J.; Tritt, T. M. Advances in Thermoelectric Materials Research: Looking Back and Moving Forward. *Science.* **2017**, 357, eaak9997.

(8) Cai, B.; Hu, H.; Zhuang, H.-L.; Li, J.-F. Promising Materials for Thermoelectric Applications. *J. Alloys Compd.* **2019**, *806*, 471–486.

(9) Witting, I. T.; Chasapis, T. C.; Ricci, F.; Peters, M.; Heinz, N. A.; Hautier, G.; Snyder, G. J. The Thermoelectric Properties of Bismuth Telluride. *Adv. Electron. Mater.* **2019**, *5*, 1800904.

(10) Jeong, M.-W.; Na, S.; Shin, H.; Park, H.-B.; Lee, H.-J.; Joo, Y.-C. Thermomechanical In Situ Monitoring of Bi_2Te_3 Thin Film and Its Relationship with Microstructure and Thermoelectric Performances. *Electron. Mater. Lett.* **2018**, *14*, 426–431.

(11) Makala, R. S.; Jagannadham, K.; Sales, B. C. Pulsed Laser Deposition of Bi_2Te_3-Based Thermoelectric Thin Films. *J. Appl. Phys.* **2003**, *94*, 3907–3918.

(12) Bo, X.; Tang, A.; Dou, M.; Li, Z.; Wang, F. Controllable Electrodeposition and Mechanism Research of Nanostructured Bi_2Te_3 Thin Films with High Thermoelectric Properties. *Appl. Surf. Sci.* **2019**, *486*, 65–71.

(13) Soliman, L. I.; Nassary, M. M.; Shaban, H. T.; Salwa, A. S. Influence of Se on the Electron Mobility in Thermal Evaporated $Bi_2(Te_{1-x}Se_x)_3$ Thin Films. *Vacuum* **2010**, *85*, 358–364.

(14) Vieira, E. M. F.; Figueira, J.; Pires, A. L.; Grilo, J.; Silva, M. F.; Pereira, A. M.; Goncalves, L. M. Enhanced Thermoelectric Properties of Sb_2Te_3 and Bi_2Te_3 Films for Flexible Thermal Sensors. *J. Alloys Compd.* **2019**, *774*, 1102–1116..

(15) Choi, H.; Jeong, K.; Chae, J.; Park, H.; Baeck, J.; Kim, T. H.; Song, J. Y.; Park, J.; Jeong, K.-H.; Cho, M.-H. Enhancement in Thermoelectric Properties of Te-Embedded Bi_2Te_3 by Preferential Phonon Scattering in Heterostructure Interface. *Nano Energy* **2018**, *47*, 374–384.

(16) Rojas, J. P.; Singh, D.; Inayat, S. B.; Sevilla, G. A. T.; Fahad, H. M.; Hussain, M. M. Review—Micro and Nano-Engineering Enabled New Generation of Thermoelectric Generator Devices and Applications. *ECS J. Solid State Sci. Technol.* **2017**, *6*, N3036–N3044.

(17) Nozariasbmarz, A.; Collins, H.; Dsouza, K.; Polash, M. H.; Hosseini, M.; Hyland, M.; Liu, J.; Malhotra, A.; Ortiz, F. M.; Mohaddes, F.; Ramesh, V. P.; Sargolzaeiaval, Y.; Snouwaert, N.; Özturk, M. C.; Vashaee, D. Review of Wearable Thermoelectric Energy Harvesting: From Body Temperature to Electronic Systems. *Appl. Energy* **2020**, *258*, 114069.

(18) Tainoff, D.; Proudhom, A.; Tur, C.; Crozes, T.; Dufresnes, S.; Dumont, S.; Bourgault, D.;

Bourgeois, O. Network of Thermoelectric Nanogenerators for Low Power Energy Harvesting. *Nano Energy* **2019**, *57*, 804–810.

(19) Yuan, Z.; Tang, X.; Xu, Z.; Li, J.; Chen, W.; Liu, K.; Liu, Y.; Zhang, Z. Screen-Printed Radial Structure Micro Radioisotope Thermoelectric Generator. *Appl. Energy* **2018**, *225*, 746–754.

(20) Mu, X.; Zhu, W.; Zhao, W.; Zhou, H.; Sun, Z.; Li, C.; Ma, S.; Wei, P.; Nie, X.; Yang, J.; Zhang, Q. Excellent Transverse Power Generation and Cooling Performances of Artificially Tilted Thermoelectric Film Devices. *Nano Energy* **2019**, *66*, 104145.

(21) Xu, Z.; Li, J.; Tang, X.; Liu, Y.; Jiang, T.; Yuan, Z.; Liu, K. Electrodeposition Preparation and Optimization of Fan-Shaped Miniaturized Radioisotope Thermoelectric Generator. *Energy* **2020**, *194*, 116873.

(22) Liu, S.; Hu, B.; Liu, D.; Li, F.; Li, J.-F.; Li, B.; Li, L.; Lin, Y.-H.; Nan, C.-W. Micro-Thermoelectric Generators Based on through Glass Pillars with High Output Voltage Enabled by Large Temperature Difference. *Appl. Energy* **2018**, *225*, 600–610.

(23) Feng, R.; Tang, F.; Zhang, N.; Wang, X. Flexible, High-Power Density, Wearable Thermoelectric Nanogenerator and Self-Powered Temperature Sensor. *ACS Appl. Mater. Interfaces* **2019**, *11* (42), 38616–38624.

(24) Fourmont, P.; Gerlein, L. F.; Fortier, F.-X.; Cloutier, S. G.; Nechache, R. Highly Efficient Thermoelectric Microgenerators Using Nearly Room Temperature Pulsed Laser Deposition. *ACS Appl. Mater. Interfaces* **2018**, *10*, 10194–10201.

(25) Hu, Z.; Gao, S. Upper Crustal Abundances of Trace Elements: A Revision and Update. *Chem. Geol.* **2008**, *253*, 205–221.

(26) Hu, G.; Edwards, H.; Lee, M. Silicon Integrated Circuit Thermoelectric Generators with a High Specific Power Generation Capacity. *Nat. Electron.* **2019**, *2*, 300–306.

(27) Domnez Noyan, I.; Gadea, G.; Salleras, M.; Pacios, M.; Calaza, C.; Stranz, A.; Dolcet, M.; Morata, A.; Tarancon, A.; Fonseca, L. SiGe Nanowire Arrays Based Thermoelectric Microgenerator. *Nano Energy* **2019**, *57*, 492–499.

(28) Su, Y.; Lu, J.; Villaroman, D.; Li, D.; Huang, B. Free-Standing Planar Thermoelectric Microrefrigerators Based on Nano-Grained SiGe Thin Films for on-Chip Refrigeration. *Nano Energy* **2018**, *48*, 202–210.

(29) Choi, J.; Cho, K.; Kim, S. Flexible Thermoelectric Generators Composed of N-and p-Type Silicon Nanowires Fabricated by Top-Down Method. *Adv. Energy Mater.* **2017**, *7*, 1602138.

(30) Lee, C. W.; Kim, G. H.; Choi, J. W.; An, K.-S.; Kim, J.-S.; Kim, H.; Lee, Y. K. Improvement of Thermoelectric Properties of Bi_2Te_3 and Sb_2Te_3 Films Grown on Graphene Substrate. *Phys. status solidi - Rapid Res. Lett.* **2017**, *11*, 1700029.

(31) de Groot, C. H.; Gurnani, C.; Hector, A. L.; Huang, R.; Jura, M.; Levason, W.; Reid, G.

Highly Selective Chemical Vapor Deposition of Tin Diselenide Thin Films onto Patterned Substrates via Single Source Diselenoether Precursors. *Chem. Mater.* **2012**, *24*, 4442–4449.

(32) Benjamin, S. L.; de Groot, C. H.; Gurnani, C.; Hector, A. L.; Huang, R.; Ignatyev, K.; Levason, W.; Pearce, S. J.; Thomas, F.; Reid, G. Area Selective Growth of Titanium Diselenide Thin Films into Micropatterned Substrates by Low-Pressure Chemical Vapor Deposition. *Chem. Mater.* **2013**, *25*, 4719–4724.

(33) Benjamin, S. L.; de Groot, C. H.; Gurnani, C.; Hector, A. L.; Huang, R.; Koukharenko, E.; Levason, W.; Reid, G. Controlling the Nanostructure of Bismuth Telluride by Selective Chemical Vapour Deposition from a Single Source Precursor. *J. Mater. Chem. A* **2014**, *2*, 4865–4869.

(34) Benjamin, S. L.; de Groot, C. H.; Hector, A. L.; Huang, R.; Koukharenko, E.; Levason, W.; Reid, G. Chemical Vapour Deposition of Antimony Chalcogenides with Positional and Orientational Control: Precursor Design and Substrate Selectivity. *J. Mater. Chem. C* **2015**, *3*, 423–430.

(35) Benjamin, S. L.; de Groot, C. H. (Kees); Gurnani, C.; Hawken, S. L.; Hector, A. L.; Huang, R.; Jura, M.; Levason, W.; Reid, E.; Reid, G.; Richards, S. P.; Stenning, G. B. G. Compositionally Tunable Ternary Bi 2 (Se 1−x Te x) 3 and (Bi 1−y Sb y) 2 Te 3 Thin Films via Low Pressure Chemical Vapour Deposition. *J. Mater. Chem. C* **2018**, *6*, 7734–7739.

(36) Huang, R.; Benjamin, S. L.; Gurnani, C.; Wang, Y.; Hector, A. L.; Levason, W.; Reid, G.; De Groot, C. H. (Kees). Nanoscale Arrays of Antimony Telluride Single Crystals by Selective Chemical Vapor Deposition. *Sci. Rep.* **2016**, *6*, 27593.

(37) Zhu, T.; Liu, Y.; Fu, C.; Heremans, J. P.; Snyder, J. G.; Zhao, X. Compromise and Synergy in High-Efficiency Thermoelectric Materials. *Adv. Mater.* **2017**, *29*, 1605884.

(38) Anderson, T. L.; Krause, H. B. Refinement of the Sb_2Te_3 and Sb_2Te_2Se Structures and Their Relationship to Nonstoichiometric $Sb_2Te_{3-y}Se_y$ Compounds. *Acta Crystallogr. Sect. B Struct. Crystallogr. Cryst. Chem.* **1974**, *30*, 1307–1310.

(39) ICSD: Inorganic Crystal Structure Database (ICSD), Fachin- Formationszentrum Karlsruhe (FIZ), Accessed via the EPSRC National Chemical Database Service Hosted by the Royal Society of Chemistry.

(40) Zhu, T.; Hu, L.; Zhao, X.; He, J. New Insights into Intrinsic Point Defects in V_2VI_3 Thermoelectric Materials. *Adv. Sci.* **2016**, *3*, 1600004.

(41) Yang, H. Q.; Chen, Y. J.; Wang, X. Y.; Miao, L.; Li, X. Y.; Han, X. D.; Lu, X.; Wang, G. Y.; Zhou, X. Y. Realizing High Thermoelectric Performance in Te Nanocomposite through Sb_2Te_3 Incorporation. *CrystEngComm* **2018**, *20*, 7729–7738.

(42) Lee, M. H.; Kim, K. R.; Rhyee, J. S.; Park, S. D.; Snyder, G. J. High Thermoelectric Figure-of-Merit in Sb2Te3/Ag2Te Bulk Composites as Pb-Free p-Type Thermoelectric Materials. *J. Mater. Chem. C* **2015**, *3*, 10494–10499.

(43) Heremans, J. P.; Wiendlocha, B.; Chamoire, A. M. Resonant Levels in Bulk Thermoelectric Semiconductors. *Energy and Environmental Science*. **2012,** *5*, 5510–5530.

(44) Snyder, G. J.; Toberer, E. S. Complex Thermoelectric Materials. *Nat. Mater.* **2008**, *7*, 105–114.

(45) Gayner, C.; Kar, K. K. Recent Advances in Thermoelectric Materials. *Prog. Mater. Sci.* **2016**, *83*, 330–382.

(46) Wang, G.; Shi, H.; Lotnyk, A.; Shi, D.; Wang, R. Conversion of p–n Conduction Type by Spinodal Decomposition in Zn-Sb-Bi Phase-Change Alloys. *NPG Asia Mater.* **2020**, *12*, 17.

(47) Asfandiyar; Cai, B.; Zhuang, H.-L.; Tang, H.; Li, J.-F. Polycrystalline SnSe–$Sn_{1-v}S$ Solid Solutions: Vacancy Engineering and Nanostructuring Leading to High Thermoelectric Performance. *Nano Energy* **2020**, *69*, 104393.

(48) Wu, Z.; Mu, E.; Wang, Z.; Chen, X.; Wu, Z.; Liu, Y.; Hu, Z. Bi_2Te_3 Nanoplates' Selective Growth Morphology on Different Interfaces for Enhancing Thermoelectric Properties. *Cryst. Growth Des.* **2019**, *19*, 3639–3646.

(49) Kumar, M.; Vora-ud, A.; Seetawan, T.; Han, J. G. Thermoelectric Power Factor Enhancement by Pulsed Plasma Engineering in Magnetron Sputtering Induced $Ge_2Sb_2Te_5$ Thin Films. *ACS Appl. Energy Mater.* **2018**, *1* (8), 4025–4031.

(50) Chen, Z.; Zhang, X.; Pei, Y. Manipulation of Phonon Transport in Thermoelectrics. *Adv. Mater.* **2018**, *30*, 1705617.

(51) Kim, H.-S.; Gibbs, Z. M.; Tang, Y.; Wang, H.; Snyder, G. J. Characterization of Lorenz Number with Seebeck Coefficient Measurement. *APL Mater.* **2015**, *3*, 041506.

Toc graphic

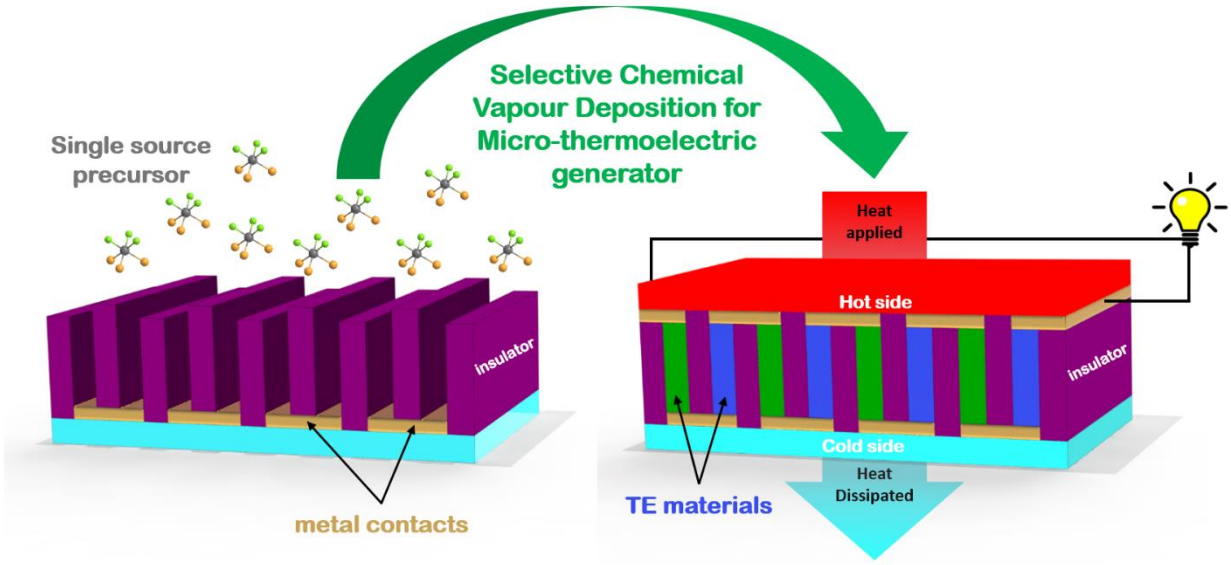
Selective Chemical
Vapour Deposition for
Micro-thermoelectric
generator
Single source
precursor
insulator
metal contacts
Heat
applied
Hot side
insulator
Cold side
Heat
Dissipated
TE materials